

## Coexistence of low-frequency spin-torque ferromagnetic resonance and unidirectional spin Hall magnetoresistance

Motomi Aoki,<sup>1</sup> Ei Shigematsu,<sup>1</sup> Ryo Ohshima,<sup>1</sup> Teruya Shinjo,<sup>1</sup> Masashi Shiraishi,<sup>1</sup> and Yuichiro Ando<sup>1,2,\*</sup>

<sup>1</sup>*Department of Electronic Science and Engineering, Kyoto University, Kyoto 615-8510, Japan*

<sup>2</sup>*PRESTO, Japan Science and Technology Agency, Honcho, Kawaguchi, Saitama 332-0012, Japan*



(Received 8 March 2021; revised 2 August 2021; accepted 16 August 2021; published 1 September 2021)

We investigate the DC voltage under an applied microwave current for platinum(Pt)/cobalt(Co), tantalum(Ta)/Co, and tungsten(W)/Co bilayers, where the microwave-induced alternating magnetic field ( $B_{\text{rf}}$ ) is parallel to an external static magnetic field ( $B_{\text{ext}}$ ). Whereas spin torque ferromagnetic resonance (ST FMR) signals do not appear because of the parallel configuration of  $B_{\text{rf}}$  and the magnetization of the Co layer, we recently found a clear hysteresis signal around  $B_{\text{ext}} = 0$  mT only when the microwave frequency ( $f_{\text{MW}}$ ) is low, typically less than 10 GHz. This low-frequency ST FMR (LFST FMR) signal enables us to detect magnetization switching induced by spin-orbit torque (SOT) with high sensitivity. In this study, we found an additional background (BG) signal superimposed on the LSFT FMR signal. The additional BG signal also has hysteresis behavior and appears even at high  $f_{\text{MW}}$ , where the LSFT FMR signal completely disappears. The sign of the BG signal is changed by changing the nonmagnetic material from Pt to Ta or W. By measuring  $f_{\text{MW}}$ , the microwave current, the temperature, and the magnetic field angle dependences, we conclude that the BG signal is induced by spin-dependent unidirectional spin Hall magnetoresistance (SD USMR), which is generated by a spin current induced by the spin Hall effect of nonmagnetic metals and spin-dependent electron mobility in ferromagnetic metals. The SD USMR signal appears in wide ranges of  $f_{\text{MW}}$  and  $B_{\text{ext}}$  because the SD USMR originates from the nonlinearity of current-dependent resistance and is not related to magnetization dynamics. From the magnitude of the BG signal, the spin Hall angles of Pt and Ta are calculated to be  $0.026 \pm 0.006$  and  $-0.042 \pm 0.006$ , respectively. In addition, we demonstrate SOT magnetization switching using the BG signal.

DOI: [10.1103/PhysRevB.104.094401](https://doi.org/10.1103/PhysRevB.104.094401)

### I. INTRODUCTION

Spin-orbit torque (SOT) is one of the most attractive research areas of spintronics [1,2] because it enables low power consumption and highly enduring magnetization switching in magnetoresistive random access memory (MRAM). A material with a large spin Hall angle,  $\theta_{\text{SH}}$ , is essential for efficient writing of MRAM using SOT. Therefore, many researchers have experimentally investigated  $\theta_{\text{SH}}$  for various materials [3–13]. Spin torque ferromagnetic resonance (ST FMR) is one of the most widely used methods for evaluating  $\theta_{\text{SH}}$  [14]. In this method, an alternating current,  $I_{\text{rf}}$ , for generation of microwaves is injected into a nonmagnetic metal (NM)/ferromagnetic metal (FM) bilayer under an applied static magnetic field  $B_{\text{ext}}$ . A microwave alternating magnetic field,  $B_{\text{rf}}$ , and/or SOT generated by the spin Hall effect (SHE) in the NM layer induces precession of the magnetization of the FM layer. The magnetization precession is converted into an oscillation of the resistance of the NM/FM bilayer,  $R_{\text{NM/FM}}$ , via the anisotropic magnetoresistance (AMR) of the FM layer. The oscillating  $R_{\text{NM/FM}}$  and  $I_{\text{rf}}$  generate a DC voltage,  $V_{\text{DC}}$ , whose amplitude is maximized around the ferromagnetic

resonance (FMR) condition.  $\theta_{\text{SH}}$  is estimated by analyzing the  $V_{\text{DC}}-B_{\text{ext}}$  spectra. Note that the ST FMR does not generally appear when a sufficiently large  $B_{\text{ext}}$  is applied perpendicular to the direction of  $I_{\text{rf}}$  because neither  $B_{\text{rf}}$  nor the SOT induces a torque on the magnetization. On the contrary, recently we found that a strong DC voltage is also generated even when  $B_{\text{ext}}$  is perpendicular to the direction of  $I_{\text{rf}}$ , especially when the microwave frequency,  $f_{\text{MW}}$ , is less than 10 GHz. This is called low-frequency ST FMR (LFST FMR) [15]. The LFST FMR generally appears at low  $B_{\text{ext}}$ . The origin of the LFST FMR is the finite slope in a  $R_{\text{NM/FM}}-B_{\text{ext}}$  curve around  $B_{\text{ext}} = 0$  mT [16]. Because the magnetic domain structure is not uniform around  $B_{\text{ext}} = 0$  mT, particularly at the edge of the FM layer owing to the shape anisotropy, the total magnetization of the whole FM layer at positive  $I_{\text{rf}}$  is different from that at negative  $I_{\text{rf}}$ . This results in oscillation of  $R_{\text{NM/FM}}$  and generation of  $V_{\text{DC}}$ .

LFST FMR is expected to accelerate investigations of SOT materials because it enables highly sensitive detection of SOT-induced magnetization switching of the FM layer with in-plane magnetic anisotropy without complicated device fabrication. Actually, magnetization switching of 100 nm wide ferromagnetic electrodes was successfully demonstrated owing to the high sensitivity. However, the origin of LFST FMR has not been completely revealed. The obtained LFST FMR spectrum was approximately a factor of 2 larger than the one calculated in our previous research [15]. Although the magnitude of the LFST FMR was shown to depend on

\*Present address: A1-226, Kyodai Katsura, Nishikyo-ku, Kyoto, Japan; corresponding author: ando.yuichiro.5s@kyoto-u.ac.jp

the slope of the  $R_{\text{NM}/\text{FM}}-B_{\text{ext}}$  curve, it still deviated from the calculation [17]. Therefore, a contribution to the LFST FMR spectrum other than from the  $R_{\text{NM}/\text{FM}}-B_{\text{ext}}$  slope is expected.

In this study, we found an additional background (BG) signal superimposed on the LFST FMR spectra and even on the ST FMR spectra. We concluded that this BG signal is generated by the unidirectional spin Hall magnetoresistance (USMR) caused by the SHE in the NM layer [18–23]. In the USMR, the spin-dependent interfacial and/or bulk resistance of the FM layer and spin-dependent electron mobility play an important role in generating  $V_{\text{DC}}$ . In an NM/FM bilayer with a finite spin-orbit coupling of the NM layer, a spin current generated by the SHE in the NM layer is injected into the FM layer. The spin polarization of this spin current is reversed depending on the polarity of  $I_{\text{rf}}$ . In this situation, the total resistance also has a nonlinear  $I_{\text{rf}}$  dependence, resulting in generation of  $V_{\text{DC}}$ . By measuring  $f_{\text{MW}}$ , the amplitude of  $I_{\text{rf}}$ , the temperature, and magnetic field angle dependences of the BG signal, we concluded that the origin of the BG signal is the spin-dependent USMR (SD USMR) [22]. The magnitude of the SD USMR has been theoretically investigated and calculated using the spin diffusion equation [20]. From the magnitude of the BG signal, we estimated  $\theta_{\text{SH}}$  for Pt and Ta to be  $0.026 \pm 0.006$  and  $-0.042 \pm 0.006$ , respectively. We also detected SOT magnetization switching using the hysteresis characteristics of the BG signal. Because the SD USMR is induced by the spin-dependent conductivity of the FM and is not related to spin torque or magnetization dynamics, we successfully detected magnetization switching even when  $f_{\text{MW}}$  was high at 13 GHz. The threshold current density was  $3 \times 10^7$  A/cm<sup>2</sup>, which is consistent with previous research ( $1.8 \times 10^7$  A/cm<sup>2</sup>) [24]. Under a specific condition, we can enhance  $V_{\text{DC}}$  using both the LFST FMR and the SD USMR, which enables more efficient detection of the magnetization switching. The SD USMR is also superimposed on the ST FMR signals because it appears universally irrespective of  $f_{\text{MW}}$ , magnetic field angle, and device geometry. Once the parameters such as spin diffusion length, polarization of the electron mobility, and the anomalous Nernst voltage are obtained by additional experiments, this allows us to estimate  $\theta_{\text{SH}}$  from two different perspectives, i.e., spin torque and spin-dependent magnetoresistance, by only measuring one FMR spectrum, which enables the cross-check and more reliable evaluation of  $\theta_{\text{SH}}$ .

## II. SAMPLE FABRICATION AND EXPERIMENTAL PROCEDURE

Figure 1(a) shows a schematic of the device structure and electric circuit in this study. First, rectangular  $\text{NM}(t_{\text{N}})/\text{Co}(t_{\text{F}})/\text{SiO}_2(t_{\text{cap}})$  layers were fabricated via electron beam lithography and rf magnetron sputtering. The quantities  $t_{\text{N}}$ ,  $t_{\text{F}}$ , and  $t_{\text{cap}}$  are the thicknesses of the NM, Co, and  $\text{SiO}_2$  layers in nanometers (nm), respectively. Then, a rectangular ferromagnetic  $\text{Co}/\text{SiO}_2$  region with width  $w$  and length  $l$  was fabricated using electron beam lithography and argon ion ( $\text{Ar}^+$ ) milling. The  $\text{Ar}^+$  milling was stopped after etching of a  $\sim 2$  nm NM layer to make the lead line of the remaining NM later. After an additional  $\text{Ar}^+$  milling to remove the surface oxidized layer

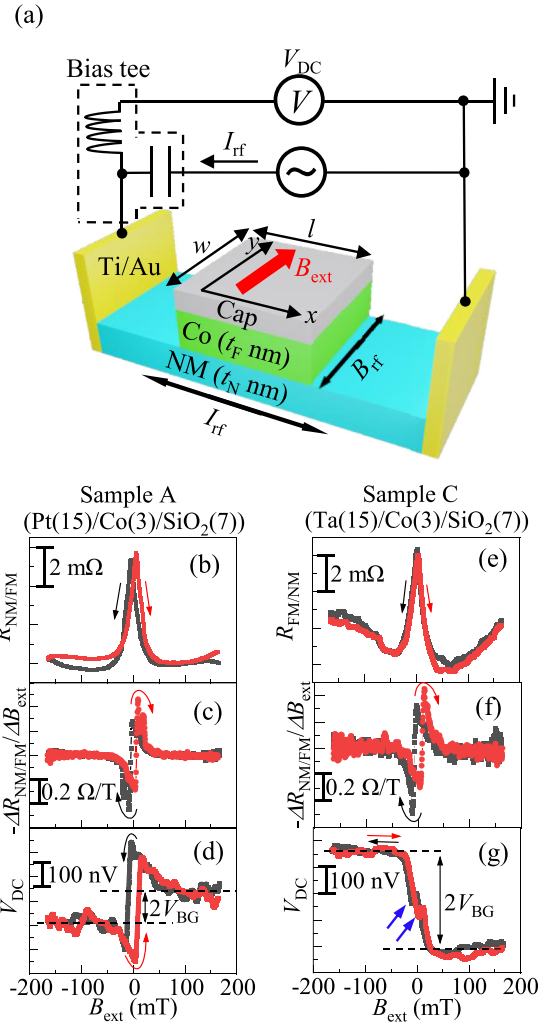


FIG. 1. (a) Schematic of the device structure and the electrical circuit used in this study. (b,e)  $R_{\text{NM}/\text{FM}}$ , (c,f)  $-\frac{\Delta R_{\text{NM}/\text{FM}}}{\Delta B_{\text{ext}}}$ , and (d,g)  $V_{\text{DC}}$  as a function of  $B_{\text{ext}}$  along the  $y$  axis for samples A and C, respectively.  $V_{\text{DC}}$  was measured under microwave irradiation with  $f_{\text{MW}} = 0.2$  GHz and microwave power  $P_{\text{MW}} = 5$  dBm ( $I_{\text{rf}}^0 = 4.5$  mA for sample A and 5.2 mA for sample C).

of the NM lead line, a Ti (3 nm)/Au (70 nm) electrode was deposited via electron beam deposition without breaking vacuum. We prepared several  $\text{NM}(t_{\text{N}})/\text{Co}(t_{\text{F}})/\text{SiO}_2(t_{\text{cap}})$  samples with various geometries and materials as follows: Pt(15)/Co(3)/SiO<sub>2</sub>(7) (sample A,  $w = 5 \mu\text{m}$ ,  $l = 0.8 \mu\text{m}$ ), Pt(15)/Co(3)/SiO<sub>2</sub>(7) (sample B,  $w = 40 \mu\text{m}$ ,  $l = 40 \mu\text{m}$ ), Ta(15)/Co(3)/SiO<sub>2</sub>(7) (sample C,  $w = 5 \mu\text{m}$ ,  $l = 1 \mu\text{m}$ ), Ta(15)/Co(8)/SiO<sub>2</sub>(7) (sample D,  $w = 10 \mu\text{m}$ ,  $l = 1.3 \mu\text{m}$ ), Ta(15)/Co(3)/SiO<sub>2</sub>(7) (sample E,  $w = 40 \mu\text{m}$ ,  $l = 40 \mu\text{m}$ ), and W(6)/Co(1)/SiO<sub>2</sub>(3) (sample F,  $w = 5 \mu\text{m}$ ,  $l = 5 \mu\text{m}$ ), as summarized in Table I. Microwave radiation with a power  $P_{\text{MW}}$  was applied via an analog commercial signal generator (Keysight N5173B EXG).  $V_{\text{DC}}$  was measured using a voltmeter (Keithley Nanovoltmeter 2182A). To demonstrate SOT magnetization switching, a 1  $\mu\text{s}$  wide pulse current was injected using a function generator (Keysight 33622A) to switch the magnetization. We used a physical property measurement system [(PPMS) Quantum Design] to measure

TABLE I. Materials and geometries of samples A–F.

| Sample | NM | $t_N$ (nm) | $t_F$ (nm) | $t_{\text{cap}}$ (nm) | $w$ ( $\mu\text{m}$ ) | $l$ ( $\mu\text{m}$ ) |
|--------|----|------------|------------|-----------------------|-----------------------|-----------------------|
| A      | Pt | 15         | 3          | 7                     | 5                     | 0.8                   |
| B      | Pt | 15         | 3          | 7                     | 40                    | 40                    |
| C      | Ta | 15         | 3          | 7                     | 5                     | 1                     |
| D      | Ta | 15         | 8          | 7                     | 10                    | 1.3                   |
| E      | Ta | 15         | 3          | 7                     | 40                    | 40                    |
| F      | W  | 6          | 1          | 3                     | 5                     | 5                     |

the  $V_{\text{DC}}-B_{\text{ext}}$  curves at low temperature.  $V_{\text{DC}}$  was measured using a voltmeter (Keithley Nanovoltmeter 2182A) under microwave irradiation generated by a function generator (Keysight 33622A) with a frequency of 0.1 GHz. The amplitude of the voltage for generating  $I_{\text{rf}}$ ,  $V_{\text{MW}}$ , was fixed to 2 V peak to peak.  $B_{\text{ext}}$  was applied along the  $y$  axis as shown in Fig. 1(a). The experiments were carried out at room temperature unless otherwise indicated.

### III. RECTIFICATION SIGNAL UNDER MICROWAVE IRRADIATION

When  $f_{\text{MW}}$  is lower than the ferromagnetic resonance (FMR) frequency, a nonzero  $V_{\text{DC}}$  is generated around  $B_{\text{ext}} = 0$  mT via the oscillation of  $R_{\text{NM}/\text{FM}}$  due to the LFST FMR [15].  $V_{\text{DC}}$  generated by the LFST FMR,  $V_{\text{LF}}$ , is expressed as

$$V_{\text{LF}} = \frac{1}{2} I_{\text{rf}}^0 B_{\text{eff}}^0 \frac{\Delta R_{\text{NM}/\text{FM}}}{\Delta B_{\text{ext}}}, \quad (1)$$

where definitions of  $I_{\text{rf}}^0$  and  $B_{\text{eff}}^0$  are  $I_{\text{rf}} = I_{\text{rf}}^0 \sin 2\pi f_{\text{MW}} t$  and  $B_{\text{eff}} = B_{\text{eff}}^0 \sin 2\pi f_{\text{MW}} t$ , respectively.  $B_{\text{eff}}$  is composed of  $B_{\text{rf}}$  induced by the part of  $I_{\text{rf}}$  flowing through the NM layer and the spin Hall effective field,  $B_{\text{SH}}$ , corresponding to the fieldlike torque SOT.  $\Delta B_{\text{ext}}$  is the peak to peak value of  $B_{\text{rf}} + B_{\text{SH}}$ , and  $|B_{\text{rf}}| > |B_{\text{SH}}|$  was confirmed in this study. Considering that the signs of  $I_{\text{rf}}$  and  $B_{\text{rf}}$  are always opposite in our device structure,  $V_{\text{LF}}$  is proportional to  $-\frac{\Delta R_{\text{NM}/\text{FM}}}{\Delta B_{\text{ext}}}$ . The contribution of dampinglike torque SOT is negligible for generating  $V_{\text{LF}}$ , because the phase difference between the oscillating magnetization and  $I_{\text{rf}}$  is almost  $0^\circ$  when  $f_{\text{MW}}$  is sufficiently low compared with that for the FMR conditions. Figures 1(b)–1(d) show the  $B_{\text{ext}}$  dependences of (b)  $R_{\text{NM}/\text{FM}}$ , which was obtained by monitoring DC voltage with an application of a DC charge current; (c)  $-\frac{\Delta R_{\text{NM}/\text{FM}}}{\Delta B_{\text{ext}}}$ ; and (d) the rectification voltage under microwave,  $V_{\text{DC}}$ , for sample A. Here,  $\Delta B_{\text{ext}}$  was set to 0.2 mT. The shape of the  $V_{\text{DC}}-B_{\text{ext}}$  curve in Fig. 1(d) roughly corresponds to that of the  $-\frac{\Delta R_{\text{NM}/\text{FM}}}{\Delta B_{\text{ext}}}-B_{\text{ext}}$  curve in Fig. 1(c). Note that the signal shape of the  $-\frac{\Delta R_{\text{NM}/\text{FM}}}{\Delta B_{\text{ext}}}-B_{\text{ext}}$  curve was almost unchanged even though a different  $\Delta B_{\text{ext}}$  i.e., different  $B_{\text{SH}}$ , was employed (see the Supplemental material (SM), A [25]) Figures 1(e)–1(g) show the  $B_{\text{ext}}$  dependences of (e)  $R_{\text{NM}/\text{FM}}$ ; (f)  $-\frac{\Delta R_{\text{NM}/\text{FM}}}{\Delta B_{\text{ext}}}$ ; and (g)  $V_{\text{DC}}$  for sample C. In contrast to sample A, there are clear differences between the  $-\frac{\Delta R_{\text{NM}/\text{FM}}}{\Delta B_{\text{ext}}}-B_{\text{ext}}$  and  $V_{\text{DC}}-B_{\text{ext}}$  curves as shown in Figs. 1(f) and 1(g). For example,  $V_{\text{DC}}$  at strong positive  $B_{\text{ext}}$  is clearly lower than at strong negative  $B_{\text{ext}}$ , indicating an additional background voltage. We can recognize the LFST FMR with switching fields at

$\pm 20$  mT as indicated by the blue arrows, which correspond to the switching fields in Fig. 1(f). It seems that a BG signal with an odd function and a saturation around  $|B_{\text{ext}}| \geq 30$  mT is superimposed on the LFST FMR. The magnitude of the BG signal,  $V_{\text{BG}}$ , is defined as  $2V_{\text{BG}} = V_{\text{DC}}^+ - V_{\text{DC}}^-$ , where  $V_{\text{DC}}^+$  ( $V_{\text{DC}}^-$ ) is the average of  $V_{\text{DC}}$  at  $B_{\text{ext}} > 50$  mT ( $B_{\text{ext}} < -50$  mT). Note that the ST FMR was negligible in our measurement setup because  $B_{\text{ext}}$  was applied perpendicular to the direction of  $I_{\text{rf}}$ . Whereas relatively low  $V_{\text{BG}}$  is also recognized for sample A, its sign is opposite to that of sample C. Therefore,  $V_{\text{BG}}$  might have a relationship with  $\theta_{\text{SH}}$  because the signs of  $\theta_{\text{SH}}$  for Pt and Ta are opposite to each other. One possible origin of the BG signal is a thermoelectric effect such as the anomalous Nernst effect (ANE) [26,27] and the spin-dependent Seebeck effect (SDSE) [28–30]. Owing to the nonuniform flow of  $I_{\text{rf}}$  in the NM/FM bilayers and unequal heat conductivity between the top and bottom surfaces, a thermal gradient perpendicular to the film plane is expected to be generated [8,31]. This thermal gradient generates an electromotive force along the  $x$  direction in Fig. 1(a) whose sign depends on the magnetization direction. However, the ANE, which is dominant over the SDSE in the NM/Co bilayers, shows the same sign irrespective of  $\theta_{\text{SH}}$  for the adjacent NM [31–34] because the direction of the thermal gradient in the Co layer of the Pt/Co and the Ta/Co samples is the same due to the large heat conductance of the MgO substrate (see SM, B and SM, C [25]). Therefore, whereas a non-negligible contribution by the ANE might exist, it is not the dominant origin of the BG signal.

### IV. FREQUENCY DEPENDENCE

In this section, we investigate the large BG signal observed in the Ta/Co bilayer at various  $f_{\text{MW}}$  values. Figure 2(a) shows  $V_{\text{DC}}-B_{\text{ext}}$  curves under various  $f_{\text{MW}}$  values for sample C. Figure 2(b) shows the enlarged signal of the meshed area (from  $-40$  to  $+40$  mT) in Fig. 2(a). For  $f_{\text{MW}} > 5$  GHz, a simple hysteresis is observed where  $V_{\text{DC}}$  for the upsweep is higher than for the downsweep at  $B_{\text{ext}} = 0$  mT. In contrast, for  $f_{\text{MW}} < 3$  GHz, the hysteresis signals cross at  $|B_{\text{ext}}| \leq 5$  mT; i.e.,  $V_{\text{DC}}$  for the upsweep becomes lower than for the downsweep. The magnitude of the LFST FMR has a strong  $f_{\text{MW}}$  dependence and becomes almost zero at high  $f_{\text{MW}}$ . Because of this, the crossing of the hysteresis signals at  $f_{\text{MW}} < 3$  GHz is due to the appearance of the LFST FMR where  $V_{\text{DC}}$  for the upsweep is expected to be lower than for the downsweep at  $B_{\text{ext}} = 0$  mT, as shown in Fig. 1(f). Since the LFST FMR disappears at high  $f_{\text{MW}}$ , we found that the BG signal also shows hysteresis and appears even at higher  $f_{\text{MW}}$  for  $f_{\text{MW}} > 5$  GHz. Figures 2(c) and 2(d), respectively, show the  $V_{\text{DC}}-B_{\text{ext}}$  curves under various  $f_{\text{MW}}$  values and enlarged plots for sample D, which had a thicker Co layer. In this case, the LFST FMR became dominant for  $f_{\text{MW}} < 3$  GHz, whereas the BG signals became dominant for  $f_{\text{MW}} > 7$  GHz. At  $f_{\text{MW}} = 5$  GHz, these signals canceled each other out. The magnetoresistance of the Co/Ta bilayer induced by the AMR of the Co layer increases with increasing  $t_F$  owing to the increased contribution of the conductance of the Co layer. This enhances the LFST FMR originating from AMR for sample D. The difference in behaviors between samples C

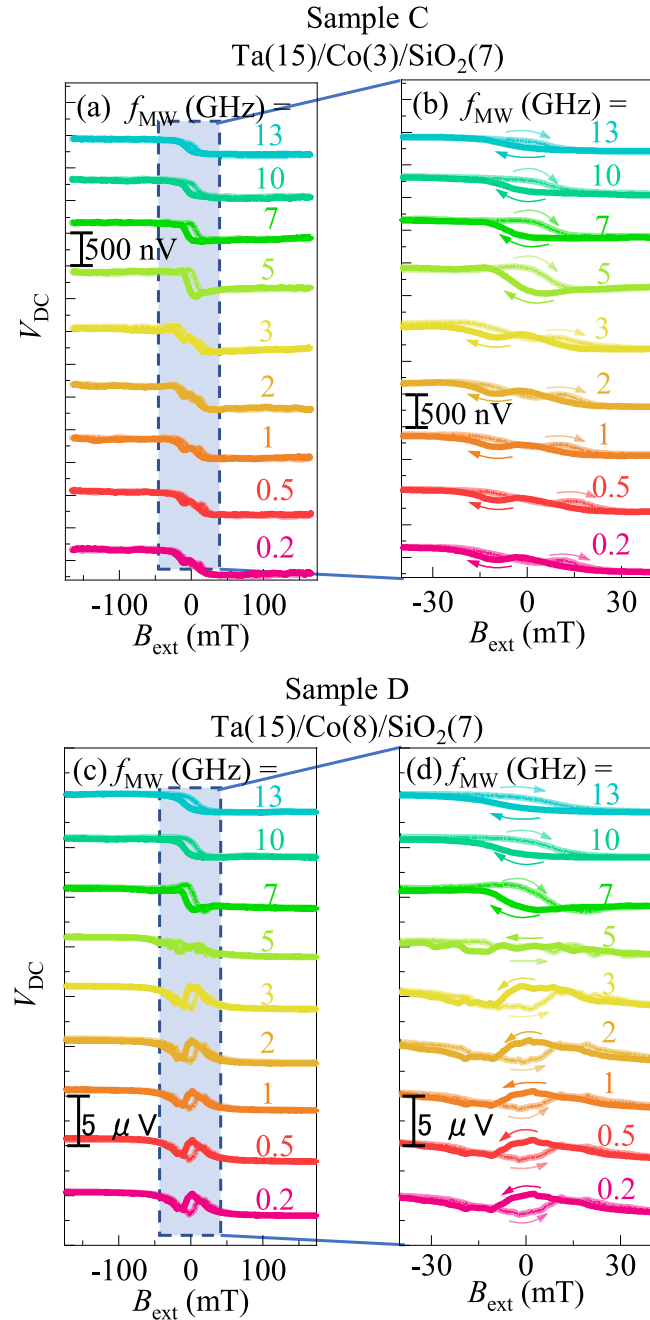


FIG. 2. (a)  $V_{DC}$  as a function of  $B_{ext}$  under various microwave frequencies,  $f_{MW}$ , and (b) enlarged  $V_{DC}$ - $B_{ext}$  curves from  $-40$  to  $+40$  mT (meshed area) for sample C.  $P_{MW}$  was 5 dBm with  $I_{rf}^0$  ranging from 4.3 mA at  $f_{MW} = 13$  GHz to 5.2 mA at  $f_{MW} = 0.2$  GHz. (c)  $V_{DC}$  as a function of  $B_{ext}$  at various  $f_{MW}$  values, and (d) enlarged plot for sample D.  $P_{MW}$  was 10 dBm, with  $I_{rf}^0$  ranging from 8 mA at  $f_{MW} = 13$  GHz to 10 mA at  $f_{MW} = 0.2$  GHz.

and D in Fig. 2 indicates that the origin of the BG signals is not directly related to AMR. Additionally,  $V_{DC}$  in the  $V_{DC}$ - $B_{ext}$  curves becomes constant at strong negative or positive  $B_{ext}$  in Fig. 2. This indicates that the BG signals do not originate from magnetization dynamics, because the magnetization is completely aligned along the  $-y$  or  $+y$  direction owing to strong  $B_{ext}$  and does not change even under microwave irradiation.

## V. DC VOLTAGE INDUCED BY UNIDIRECTIONAL SPIN HALL MAGNETORESISTANCE

The BG signal is not related to the temperature gradient, AMR, or magnetization dynamics. Therefore, we focus on the USMR [18–23], where the in-plane resistance perpendicular to the magnetization in an NM/FM structure depends on the polarity of the charge current. There are two USMR mechanisms. One is the spin-dependent USMR (SD USMR) [22], the origin of which is the spin-dependent resistance at the NM/FM interface and/or in the FM layer caused by a spin current generated via the SHE of the NM layer. In this case, the spin-dependent electron mobility generates a nonlinear magnetoresistance. The other mechanism is the spin-flip USMR (SF USMR) [22], where modulation of the magnon population due to spin injection via the SHE in the NM layer causes modulation of the electron-magnon scattering at the NM/FM interface. Typically, the magnitude of the SF USMR is suppressed at strong  $B_{ext}$  [23], which is inconsistent with the behavior obtained in Fig. 2. Therefore, the most likely origin of the BG signals is the SD USMR. From a simple spin diffusion model, the magnetoresistance induced by the SD USMR,  $R_{SDUSMR}$ , with spin-dependent electron mobility is expressed as [20]

$$R_{SDUSMR} = 6 \left( \frac{\sigma_F L_F}{\sigma_N l_N + \sigma_F l_F} \right) \times \frac{(p_\sigma - p_N) \left[ \left( \frac{\theta_{SH} L_N}{\varepsilon_F} \right) \tanh \left( \frac{l_N}{2L_N} \right) \tanh \left( \frac{l_F}{L_F} \right) \right] I R_{NM/FM}}{1 + (1 - p_\sigma^2) \left( \frac{\sigma_F L_N}{\sigma_N L_F} \right) \tanh \left( \frac{l_F}{L_F} \right) \coth \left( \frac{l_N}{L_N} \right) l}, \quad (2)$$

where  $I$ ,  $\sigma_{F(N)}$ , and  $L_{F(N)}$  are the longitudinal current, the bulk conductivity, and the spin diffusion length of the FM (NM), respectively;  $p_\sigma$  is the conductivity spin asymmetry induced by the spin-dependent electron mobility;  $p_N$  is the difference in density of states at the Fermi energy between the up and down spins; and  $\varepsilon_F$  is the Fermi energy of the FM. When  $I_{rf}$  is applied, the time average of the voltage induced by the SD USMR,  $V_{BG}$ , is expressed as

$$V_{BG} = \frac{R_{NM/FM}^2}{l} 3 \left( \frac{\sigma_F L_F}{\sigma_N l_N + \sigma_F l_F} \right) \times \frac{(p_\sigma - p_N) \left[ \left( \frac{\theta_{SH} L_N}{\varepsilon_F} \right) \tanh \left( \frac{l_N}{2L_N} \right) \tanh \left( \frac{l_F}{L_F} \right) \right] I_{rf}^2}{1 + (1 - p_\sigma^2) \left( \frac{\sigma_F L_N}{\sigma_N L_F} \right) \tanh \left( \frac{l_F}{L_F} \right) \coth \left( \frac{l_N}{L_N} \right)}. \quad (3)$$

Because the polarities of  $p_\sigma$  and  $p_N$  are changed by the magnetization reversal and their magnitudes are constant unless the magnetization direction changes,  $V_{BG}$  in Eq. (3) is consistent with the BG signals obtained in Fig. 2. Furthermore, the polarity of  $V_{BG}$  depends on  $\theta_{SH}$ , which is consistent with the polarity change of  $V_{BG}$  between samples A and C. For the LFST FMR, the DC voltage is generated by the product of the oscillating resistance due to magnetization precession and the AC current, which has the same frequency. This is the spin rectification effect. In contrast, for the SD USMR, the DC voltage is generated by the charge current dependence on magnetoresistance. Therefore, it is not related to the magneti-



zation dynamics and appears in wide ranges of  $f_{\text{MW}}$  and  $B_{\text{ext}}$ . The  $t_{\text{F}}$  dependence is also expected to be different because the magnitude of the SD USMR is maximized at a specific value that is related to  $L_{\text{F}}$ .

## VI. CURRENT, TEMPERATURE, AND ANGLE DEPENDENCES

To verify that the BG signal is actually generated by the SD USMR, we measured  $V_{\text{BG}}$  under various conditions. Figure 3(a) shows  $V_{\text{BG}}/I_{\text{rf}}^{02}$  as a function of  $f_{\text{MW}}$ . Taking into account the frequency-dependent attenuation in the measurement system because of impedance mismatch,  $I_{\text{rf}}^0$  was estimated using a vector network analyzer (Agilent E5071C). No clear relationship was found between  $V_{\text{BG}}/I_{\text{rf}}^{02}$  and  $f_{\text{MW}}$ , which is consistent with the characteristics of SD USMR. Next, we investigated the  $I_{\text{rf}}^0$  dependence of  $V_{\text{BG}}$  by changing  $P_{\text{MW}}$  from 0 to 13 dBm as shown in Fig. 3(b).  $V_{\text{BG}}$  was proportional to  $I_{\text{rf}}^{02}$ , in agreement with Eq. (3). The temperature dependence of  $V_{\text{BG}}$  was also investigated using PPMS for sample E. Figure 3(c) also shows the conjectured temperature evolution starting from 300 K of the DC voltage generated by the SF USMR using values in Ref. [22]. The DC voltage generated by the SF USMR approaches 0 V by decreasing the temperature because of the suppression of the magnon, obviously different from our results. Considering the measured temperature dependences in  $\sigma_{\text{F(N)}}$  and expected temperature dependences in  $\theta_{\text{SH}}$ ,  $L_{\text{F}}$ , and  $L_{\text{N}}$ , and the polarity of the magnetization in Co [35–37], the SD USMR in Ta/Co is expected to have a smaller temperature dependence than the SF USMR [21–23]. Note that the USMR induced by the high-energy magnon might also contribute to  $V_{\text{BG}}$  because it is constant up to  $B_{\text{ext}} \sim 5$  T [38]. However, the USMR induced by the high-energy magnon is suppressed at the low temperature, which is inconsistent with our experimental result. Therefore, the obtained temperature dependence of  $V_{\text{BG}}$  is consistent with that of the SD USMR.

We also investigated  $V_{\text{BG}}$  under a strong external magnetic field ( $B_{\text{ext}} = 2$  T) along different directions for sample E. Figures 4(a)–4(c) show the definitions of three different angles,  $\alpha$ ,  $\beta$ , and  $\gamma$ . Figure 4(d) shows the  $\alpha$ ,  $\beta$ , and  $\gamma$  dependences of  $V_{\text{BG}}$ . The solid lines are linear fits indicated by  $\sin\alpha$  and  $\sin\gamma_{\text{M}}$ , where  $\gamma_{\text{M}}$  is the angle between the magnetization and the  $y$  axis calculated using micromagnetic simulation. As shown in Fig. 4(d),  $V_{\text{BG}}$  is proportional to  $\sin\alpha$  and  $\sin\gamma_{\text{M}}$  (the  $y$  component of magnetization), which is also consistent with previous studies on SD USMR [18,19,21,39]. Note that if the origin of  $V_{\text{BG}}$  is magnon-induced USMR, it should show different angular dependences [22]. Because the frequency, current, temperature, and magnetic field angle dependences of  $V_{\text{BG}}$  were consistent with those of the SD USMR, we concluded that  $V_{\text{BG}}$  was mainly induced by the SD USMR.

## VII. DECONVOLUTION OF THE SIGNAL

Since the BG signal was mainly generated by the SD USMR, the magnitude of which is proportional to the  $y$  component of the magnetization, we can differentiate the contribution from the BG signal and the LFST FMR in all field ranges, respectively. The  $y$  component of the magneti-

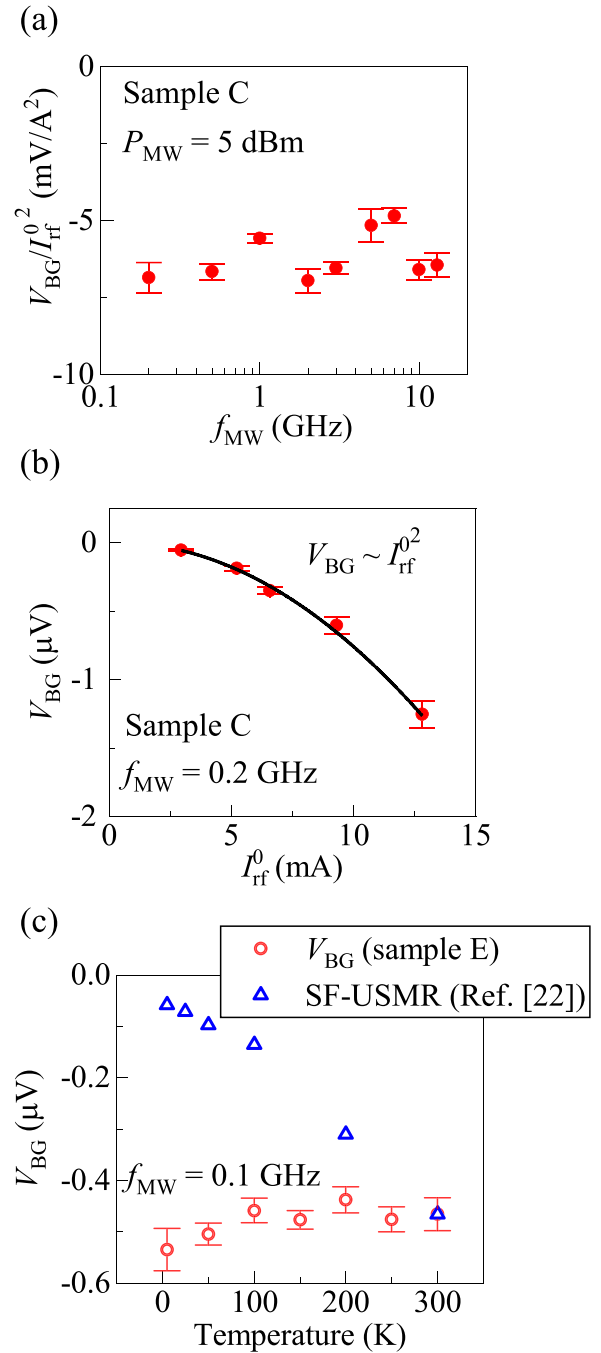


FIG. 3. (a)  $V_{\text{BG}}/I_{\text{rf}}^{02}$  as a function of  $f_{\text{MW}}$  at  $P_{\text{MW}} = 5$  dBm with  $I_{\text{rf}}^0$  ranging from 4.3 mA at  $f_{\text{MW}} = 13$  GHz to 5.2 mA at  $f_{\text{MW}} = 0.2$  GHz, and (b)  $V_{\text{BG}}$  as a function of  $I_{\text{rf}}^0$  at  $f_{\text{MW}} = 0.2$  GHz for sample C. (c)  $V_{\text{BG}}$  as a function of temperature for sample E. Under the applied voltage for microwave generation,  $V_{\text{MW}}$  and  $f_{\text{MW}}$  were 2 V ( $I_{\text{rf}}^0 = 13$  mA) and 0.1 GHz, respectively. Temperature dependence of DC voltage due to the SF USMR, where the voltage at 300 K is normalized to the same value of  $V_{\text{BG}}$  at 300 K for sample E.

zation direction was estimated from the AMR signal in the  $R_{\text{NM/FM}}-B_{\text{ext}}$  curve shown in Figs. 1(b) and 1(e). The calculated  $V_{\text{DC}}-B_{\text{ext}}$  curves due to the SD USMR for sample A and sample C are shown in Figs. 5(a) and 5(b). Clear rectangular shape signals with small rotation around switching fields were obtained. Figures 5(c) and 5(d) show the difference between

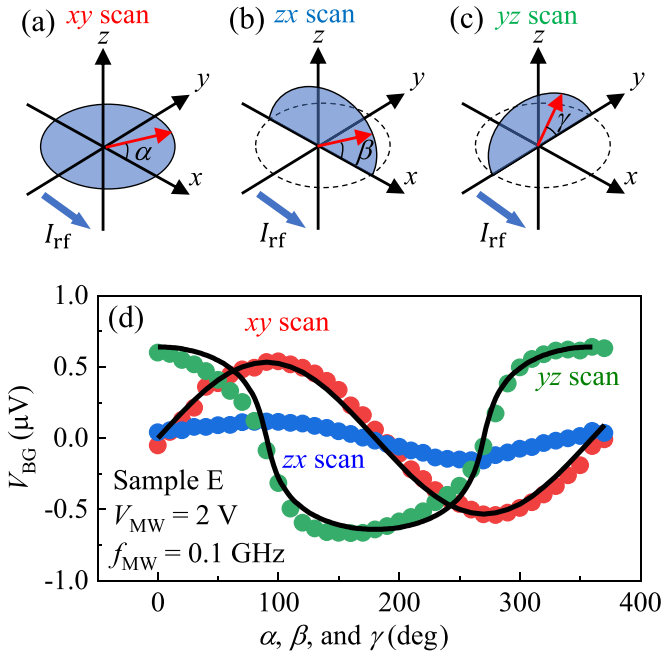


FIG. 4. (a–c) Schematics of the measurement for the magnetic field angle dependence of  $V_{BG}$ . (d)  $V_{BG}$  as a function of  $\alpha$ ,  $\beta$ , and  $\gamma$  for sample E.  $V_{MW}$  and  $f_{MW}$  were 2 V ( $I_{rf}^0 = 13$  mA) and 0.1 GHz, respectively.

experimentally obtained  $V_{DC}-B_{ext}$  curves [Figs. 1(d) and 1(g)] and the calculated  $V_{DC}-B_{ext}$  curves due to the SD USMR [Figs. 5(a) and 5(c)] for sample A and sample C, respectively. The signal shapes of Figs. 5(c) and 5(d) are both similar to those of  $-\frac{\Delta R_{NM/FM}}{\Delta B_{ext}}-B_{ext}$  curves shown in Figs. 1(c) and 1(f), respectively, indicating the dominant contribution of the LFST FMR. We found that whereas the signal shapes of Figs. 5(c) and 5(d) are almost the same for samples A and C, those of Figs. 5(a) and 5(b) exhibit finite differences in polarity and magnitude. Whereas the magnitude of the signal in Fig. 5(c) is dominant for sample A, that in Fig. 5(d) is comparable to that in Fig. 5(b) for sample C.

### VIII. DETERMINATION OF SPIN HALL ANGLE

We determined  $\theta_{SH}$  for Pt and Ta from  $V_{BG}$  measured in samples B and E. To exclude the contribution from  $V_{LF}$ , we applied a strong  $B_{ext}$  up to 1 T using PPMS and re-defined  $V_{DC}^+$  ( $V_{DC}^-$ ) as the average of  $V_{DC}$  at  $B_{ext} > 200$  mT ( $B_{ext} < -200$  mT).  $V_{MW}$  and  $f_{MW}$  were set to 2 V peak to peak and 0.1 GHz, respectively. We measured  $V_{BG}$  as  $67 \pm 15$  nV and  $-460 \pm 70$  nV for samples B and E, respectively. Although we experimentally verified that  $V_{BG}$  is mainly generated from the SD USMR, a non-negligible contribution from the ANE is also expected [18]. Therefore, we calculated the temperature gradient induced by Joule heating using COMSOL MULTIPHYSICS [34,40] and determined the resulting ANE voltage using the reported ANE coefficient (see the Supplemental Material, B [25]). As a result, the contributions from the SD USMR were estimated to be 72% and 118% of the experimentally obtained  $V_{BG}$  value for samples E and B, respectively. Using these values, we calculated  $\theta_{SH}$  for

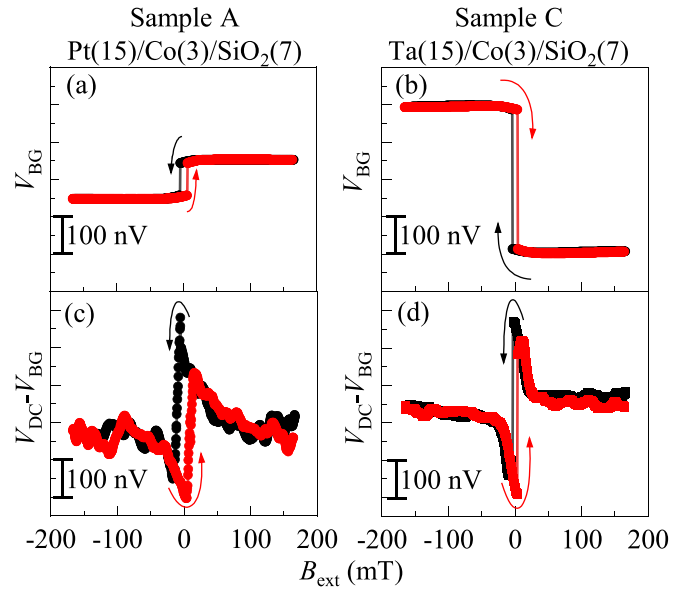


FIG. 5. Numerically calculated  $B_{ext}$  dependence of  $V_{DC}$  generated by the SD USMR for (a) sample A and (b) sample C. The  $y$  component of the magnetization was estimated from the anisotropic magnetoresistance (AMR) signal in the  $R_{NM/FM}-B_{ext}$  curve shown in Figs. 1(c) and 1(d). Difference between experimentally obtained  $V_{DC}-B_{ext}$  curves [Figs. 1(d) and 1(g)] and the calculated  $V_{DC}-B_{ext}$  curves due to the SD USMR [Figs. 5(a) and 5(c)] for (c) sample A and (d) sample C.

Ta and Pt to be  $-0.042 \pm 0.006$  and  $0.026 \pm 0.006$  from Eq. (3), respectively (see also the Supplemental Material, D [25]). The calculated value of  $\theta_{SH}$  for Ta was in the middle between the values estimated from SOT magnetization switching ( $\sim -0.12$ ) [41] and spin absorption ( $\sim -0.004$ ) [42]. The value of  $\theta_{SH}$  for Pt was smaller than that estimated from ST FMR ( $\sim 0.076$ ) [14]; however, it was consistent with that determined from spin absorption (0.021) [43] and the spin pumping (0.013) [44]. In the estimation of  $\theta_{SH}$ , the conductivities of Co, Pt, and Ta were electrically measured to be  $\sigma_F = 1.01 \times 10^6$  ( $\Omega m$ )<sup>-1</sup>,  $\sigma_{Pt} = 1.94 \times 10^6$  ( $\Omega m$ )<sup>-1</sup>,  $\sigma_{Ta} = 4.32 \times 10^5$  ( $\Omega m$ )<sup>-1</sup>. The other parameters were obtained from previous works: The spin diffusion lengths of Co, Pt, and Ta, were  $L_F = 40$  nm,  $L_{Pt} = 14$  nm, and  $L_{Ta} = 1.8$  nm [35,45]; the polarization ratio was  $p_\sigma - p_N = 0.5$ ; and the Fermi energy was  $\varepsilon_F = 5$  eV [20].  $L_F$  and  $L_N$  can also be determined by measuring the  $t_F$  and  $t_N$  dependences of  $V_{BG}$  [21], which allows us to estimate  $\theta_{SH}$  more precisely.

We emphasize that the  $V_{BG}$  signals appeared as background signals not only in the measurements of the LFST FMR but also those of the ST FMR, where  $B_{ext}$  has a finite angle from the  $y$  axis in Fig. 1(a) and the applied  $f_{MW}$  is generally high at more than several GHz (see the Supplemental Material, D [25]). In the ST FMR,  $\theta_{SH}$  is generally estimated from the ratio of the symmetric and antisymmetric components of the FMR signals, where the spin torque generated by the SHE is important. However, the unwanted effects such as the spin pumping, the ANE, the phase deviation of the magnetization oscillation, and the nonuniformity of the magnetization, sometimes hinder precise estimation. Note that  $\theta_{SH}$  can also be estimated from the background signals induced

by the SD USMR. Because the SD USMR is induced by the spin-dependent conductivity of the FM and not related to spin torque or magnetization dynamics, we can estimate  $\theta_{SH}$  from two different perspectives, i.e., spin torque and spin-dependent magnetoresistance, by measuring only one FMR spectrum. The unwanted effects are also expected to be different between these two signals. Whereas a precise estimation of the polarization of the electron mobility for the SD USMR and temperature gradient of the sample for the ANE are not so simple at this stage, it is worth cross-checking the estimated  $\theta_{SH}$  values by using both SD USMR and ST FMR signals. If we obtain a large  $\theta_{SH}$  from the amplitude ratio of the symmetric and antisymmetric components of the ST FMR signal, the BG signal should also increase.

### IX. SPIN-ORBIT TORQUE MAGNETIZATION SWITCHING

Finally, we detected SOT magnetization switching. In our previous research, we detected SOT magnetization switching using the LFST FMR [15]. However, because the detection sensitivity depends on the magnitude of the LFST FMR ( $\Delta R_{NM/FM}/\Delta B_{ext}$  at  $B_{ext} = 0$  mT), we expect it to be difficult to use when the FM layer has a low AMR ratio and/or strong coercive field. In this study, we detected SOT magnetization switching using the SD USMR. When the magnetic easy axis is along the  $y$  axis, there is a finite difference in  $V_{BG}$  at  $B_{ext} = 0$  mT between the up- and downsweeps due to magnetization hysteresis, as shown in Fig. 2. Therefore, we expect that SOT magnetization switching can be detected in the same way as in our previous research [15]. Figure 6(a) shows  $V_{DC}$  as a function of  $B_{ext}$  at various  $f_{MW}$  values for sample F. We confirmed that the SD USMR was dominant over the LFST FMR even at low  $f_{MW}$  (see the Supplemental Material, E [25]). Figure 6(b) shows a schematic of the electrical circuit for demonstrating the SOT magnetization switching. First, a strong external magnetic field,  $B_{SET}$ , was applied to initialize the magnetization of the Co layer. After removing  $B_{SET}$ , we measured the DC voltage representing the initial state of magnetization,  $V_1$ , under microwave irradiation. After microwave irradiation was stopped, a pulse current for the SOT magnetization switching was injected into the W channel. Then we measured the DC voltage representing the magnetization direction after the pulse current,  $V_2$ , under microwave irradiation. If the magnetization is successfully switched, a nonzero  $\Delta V_{PLS}$  is observed, where  $\Delta V_{PLS} = V_1 - V_2$ . Figures 6(c) and 6(d) show the enlarged spectra of  $V_{DC}$  (left panels) and  $\Delta V_{PLS}$  as functions of pulse current density  $J_{PLS}$ , i.e., the SOT magnetization switching signal (right panels), where the values of  $f_{MW}$  were 0.2 and 13 GHz, respectively. Here, the value of  $\Delta V_{PLS}$  was set to  $0 \mu V$  when the magnetization after the injection of  $J_{PLS}$  was along  $+y$  [15]. Clear hysteresis features were obtained both for  $f_{MW} = 0.2$  and 13 GHz. The magnitude of the magnetization switching signal was slightly smaller than that expected from the  $V_{DC}-B_{ext}$  curves. This is because the magnetization did not completely align along the  $+y$  or  $-y$  direction even though the maximum pulse current of our apparatus was applied. The gradual change in the hysteresis signal is mainly due to the large size of the Co layer, which is consistent with our previous study [15]. The threshold current density

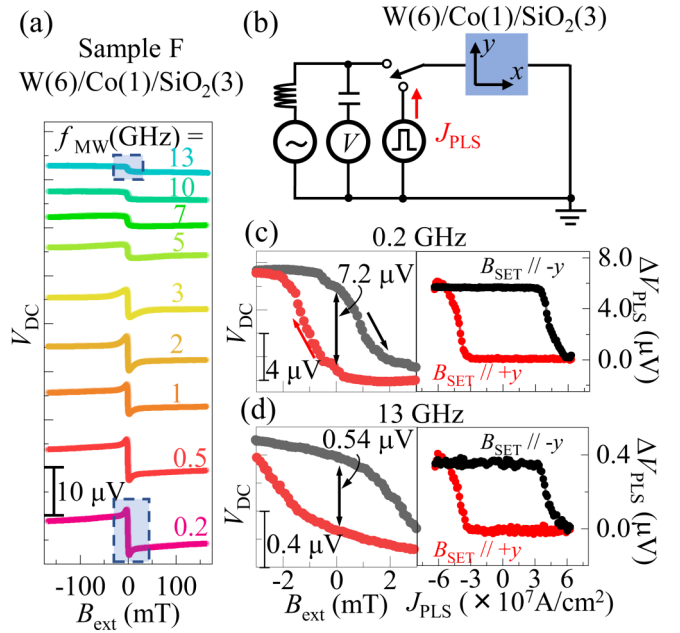


FIG. 6. (a)  $V_{DC}$  as a function of  $B_{ext}$  under microwave with various frequencies for W/Co/SiO<sub>2</sub> device with  $P_{MW} = 5$  dBm with  $I_{rf}^0$  ranging from 1.7 mA at  $f_{MW} = 13$  GHz to 2.1 mA at  $f_{MW} = 0.2$  GHz. (b) A schematic of the electrical circuit for demonstration of the magnetization switching. (c,d) Enlarged  $V_{DC}-B_{ext}$  curves between  $-3$  and  $+3$  mT (left panels) and  $\Delta V_{PLS}$  as a function of pulse current density  $J_{PLS}$  (right panels) for (c)  $f_{MW} = 0.2$  GHz and (d) 13 GHz.

was  $3 \times 10^7$  A/cm<sup>2</sup>, which is also consistent with previous research [24]. Here we mention that the SOT magnetization switching can also be detected with an application of DC charge current utilizing the USMR [46] (see the Supplemental Material, F [25]). We emphasize that the advantage of using the rectification voltage due to the USMR is the sensitivity. If we use DC charge current, measured voltage increases as the DC charge current increases, resulting in the increment of the range of the voltmeter and the reduction of the sensitivity. In our method, measured voltage is always around zero no matter how much rf charge current is applied, which enables highly sensitive detection of the SOT magnetization switching.

In demonstrating SOT magnetization switching using the LFST FMR, one should consider the contribution of the SD USMR because it modulates the magnitude of magnetization switching signals and might conceal a signal unexpectedly. The contribution ratio of LFST FMR and SD USMR can be controlled by adjusting  $f_{MW}$ ,  $t_F$ , and  $B_{ext}$ . We emphasize that although the polarities of the LFST FMR and SD USMR signals are opposite to each other in the Ta/Co or W/Co systems, it is possible to amplify the sensitivity of SOT switching detection by combining the LFST FMR and SD USMR using suitable NM/FM bilayers. For example, the SD USMR polarity is related to the relative position of the  $d$  bands of the host and impurity of the FM layer, and can be changed by controlling the composition. The LFST FMR polarity can also be changed using the FM layer, which shows negative AMR. The deviation in magnitude from the calculation for the Pt/FM

systems we previously reported is also likely due to the SD USMR contribution.

## X. CONCLUSION

In conclusion, we found an additional BG signal superimposed on the LFST FMR. By measuring the  $f_{\text{MW}}$ ,  $I_{\text{rf}}^0$ , temperature, and magnetic field angle dependences, we concluded the origin of the BG signal to be the SD USMR. We calculated  $\theta_{\text{SH}}$  for Pt and Ta to be  $0.026 \pm 0.006$  and  $-0.042 \pm 0.006$ , respectively, using the measured values of  $V_{\text{BG}}$ . SOT magnetization switching of W/Co was also demonstrated using the hysteresis behavior of  $V_{\text{BG}}$ . Because the SD USMR has a weaker relationship with the magnetization dynamics, we demonstrated magnetization switching over a wide range of  $f_{\text{MW}}$ , even for an FM with a low AMR ratio and/or strong coercive field. Furthermore, by choosing appro-

prate FM and NM materials, we can use both the LFST FMR and the SD USMR, which enable highly efficient detection. Once the parameters in Eq. (3), spin diffusion length and the polarization of the electron mobility in the FM, are obtained and the contribution from ANE is experimentally separated, we can estimate  $\theta_{\text{SH}}$  from two different perspectives by only measuring one FMR spectrum because the BG signals appear in the ST FMR signals. This enables the cross-check and more reliable evaluation of  $\theta_{\text{SH}}$ .

The data that support the findings of this study are available from the corresponding author upon reasonable request.

## ACKNOWLEDGMENTS

This work was supported by JSPS (KAKENHI Grants No. 16H06330, No. 19H02197, No. 20H02607, and No. 20K22413), JST-PRESTO (Grant No. JPMJPR20B2).

- 
- [1] I. Mihal Miron, G. Gaudin, S. Auffret, B. Rodmacq, A. Schuhl, S. Pizzini, J. Vogel, and P. Gambardella, Current-driven spin torque induced by the Rashba effect in a ferromagnetic metal layer, *Nat. Mater.* **9**, 230 (2010).
- [2] I. M. Miron, K. Garello, G. Gaudin, P.-J. Zermatten, M. V. Costache, S. Auffret, S. Bandiera, B. Rodmacq, A. Schuhl, and P. Gambardella, Perpendicular switching of a single ferromagnetic layer induced by in-plane current Injection, *Nature (London, U. K.)* **476**, 189 (2011).
- [3] Y. K. Kato, Observation of the spin Hall effect in semiconductors, *Science* **306**, 1910 (2004).
- [4] S. O. Valenzuela and M. Tinkham, Direct electronic measurement of the spin Hall effect, *Nature (London, U. K.)* **442**, 176 (2006).
- [5] S. Dushenko, M. Hokazono, K. Nakamura, Y. Ando, T. Shinjo, and M. Shiraishi, Tunable inverse spin Hall effect in nanometer-thick platinum films by ionic gating, *Nat. Commun.* **9**, 3118 (2018).
- [6] Y. Niimi, M. Morota, D. H. Wei, C. Deranlot, M. Basletic, A. Hamzic, A. Fert, and Y. Otani, Extrinsic Spin Hall Effect Induced by Iridium Impurities in Copper, *Phys. Rev. Lett.* **106**, 126601 (2011).
- [7] K. Ando, S. Takahashi, J. Ieda, Y. Kajiwara, H. Nakayama, T. Yoshino, K. Harii, Y. Fujikawa, M. Matsuo, S. Maekawa, and E. Saitoh, Inverse spin-Hall effect induced by spin pumping in metallic system, *J. Appl. Phys.* **109**, 103913 (2011).
- [8] K. Garello, I. M. Miron, C. O. Avci, F. Freimuth, Y. Mokrousov, S. Blügel, S. Auffret, O. Boulle, G. Gaudin, and P. Gambardella, Symmetry and magnitude of spin-orbit torques in ferromagnetic heterostructures, *Nat. Nanotechnol.* **8**, 587 (2013).
- [9] A. R. Mellnik, J. S. Lee, A. Richardella, J. L. Grab, P. J. Mintun, M. H. Fischer, A. Vaezi, A. Manchon, E.-A. Kim, N. Samarth, and D. C. Ralph, Spin-transfer torque generated by a topological insulator, *Nature (London, U. K.)* **511**, 449 (2014).
- [10] A. Tsukahara, Y. Ando, Y. Kitamura, H. Emoto, E. Shikoh, M. P. Delmo, T. Shinjo, and M. Shiraishi, Self-induced inverse spin Hall effect in permalloy at room temperature, *Phys. Rev. B* **89**, 235317 (2014).
- [11] J. Jiang, F. Tang, X. C. Pan, H. M. Liu, X. H. Niu, Y. X. Wang, D. F. Xu, H. F. Yang, B. P. Xie, F. Q. Song, P. Dudin, T. K. Kim, M. Hoesch, P. K. Das, I. Vobornik, X. G. Wan, and D. L. Feng, Signature of Strong Spin-Orbital Coupling in the Large Nonsaturating Magnetoresistance Material  $\text{WTe}_2$ , *Phys. Rev. Lett.* **115**, 166601 (2015).
- [12] C.-F. Pai, M. Mann, A. J. Tan, and G. S. D. Beach, Determination of spin torque efficiencies in heterostructures with perpendicular magnetic anisotropy, *Phys. Rev. B* **93**, 144409 (2016).
- [13] H. Emoto, Y. Ando, G. Eguchi, R. Ohshima, E. Shikoh, Y. Fuseya, T. Shinjo, and M. Shiraishi, Transport and spin conversion of multicarriers in semimetal bismuth, *Phys. Rev. B* **93**, 174428 (2016).
- [14] L. Liu, T. Moriyama, D. C. Ralph, and R. A. Buhrman, Spin-Torque Ferromagnetic Resonance Induced by the Spin Hall Effect, *Phys. Rev. Lett.* **106**, 036601 (2011).
- [15] M. Aoki, E. Shigematsu, M. Matsushima, R. Ohshima, S. Honda, T. Shinjo, M. Shiraishi, and Y. Ando, In-plane spin-orbit torque magnetization switching and its detection using the spin rectification effect at subgigahertz frequencies, *Phys. Rev. B* **102**, 174442 (2020).
- [16] X. F. Zhu, M. Harder, J. Tayler, A. Wirthmann, B. Zhang, W. Lu, Y. S. Gui, and C.-M. Hu, Nonresonant spin rectification in the absence of an external applied magnetic field, *Phys. Rev. B* **83**, 140402 (2011).
- [17] M. Aoki, E. Shigematsu, M. Matsushima, R. Ohshima, S. Honda, T. Shinjo, M. Shiraishi, and Y. Ando, Enhancement of low-frequency spin-orbit-torque ferromagnetic resonance signals by frequency tuning observed in Pt/Py, Pt/Co, and Pt/Fe Bilayers, *AIP Adv.* **11**, 025206 (2021).
- [18] C. O. Avci, K. Garello, A. Ghosh, M. Gabureac, S. F. Alvarado, and P. Gambardella, Unidirectional spin Hall magnetoresistance in ferromagnet/normal metal bilayers, *Nat. Phys.* **11**, 570 (2015).
- [19] K. Yasuda, A. Tsukazaki, R. Yoshimi, K. S. Takahashi, M. Kawasaki, and Y. Tokura, Large Unidirectional Magnetoresistance in a Magnetic Topological Insulator, *Phys. Rev. Lett.* **117**, 127202 (2016).



- [20] S. S. L. Zhang and G. Vignale, Theory of unidirectional spin Hall magnetoresistance in heavy-metal/ferromagnetic-metal bilayers, *Phys. Rev. B* **94**, 140411 (2016).
- [21] Y. Yin, D.-S. Han, M. C. H. de Jong, R. Lavrijsen, R. A. Duine, H. J. M. Swagten, and B. Koopmans, Thickness dependence of unidirectional spin-Hall magnetoresistance in metallic bilayers, *Appl. Phys. Lett.* **111**, 232405 (2017).
- [22] C. O. Avci, J. Mendil, G. S. D. Beach, and P. Gambardella, Origins of the Unidirectional Spin Hall Magnetoresistance in Metallic Bilayers, *Phys. Rev. Lett.* **121**, 087207 (2018).
- [23] I. V. Borisenko, V. E. Demidov, S. Urazhdin, A. B. Rinkevich, and S. O. Demokritov, Relation between unidirectional spin Hall magnetoresistance and spin current-driven magnon generation, *Appl. Phys. Lett.* **113**, 062403 (2018).
- [24] C.-F. Pai, L. Liu, Y. Li, H. W. Tseng, D. C. Ralph, and R. A. Buhrman, Spin transfer torque devices utilizing the giant spin Hall effect of tungsten, *Appl. Phys. Lett.* **101**, 122404 (2012).
- [25] See Supplemental Material at <http://link.aps.org/supplemental/10.1103/PhysRevB.104.094401> for more details on the contribution from the fieldlike torque SOT, calculation of the ANE voltage, coexistence of the BG signal and the ST FMR, estimation of the SHA with various frequencies, the BG signal of the W/Co device, and the measurement of the USMR using DC charge current.
- [26] W. Nernst, Ueber das auftreten electromotorischer kräfte in metallplatten, welche von einem wärmestrome durchflossen werden und sich im magnetischen felde befinden, *Ann. Phys.* **265**, 343 (1886).
- [27] J. Weischenberg, F. Freimuth, S. Blügel, and Y. Mokrousov, Scattering-independent anomalous Nernst effect in ferromagnets, *Phys. Rev. B* **87**, 060406 (2013).
- [28] A. Slachter, F. L. Bakker, J.-P. Adam, and B. J. van Wees, Thermally driven spin injection from a ferromagnet into a non-magnetic metal, *Nat. Phys.* **6**, 879 (2010).
- [29] M. Erekhinsky, F. Casanova, I. K. Schuller, and A. Sharoni, Spin-dependent Seebeck effect in non-local spin valve devices, *Appl. Phys. Lett.* **100**, 212401 (2012).
- [30] N. Yamashita, Y. Ando, H. Koike, S. Miwa, Y. Suzuki, and M. Shiraiishi, Thermally Generated Spin Signals in a Non-degenerate Silicon Spin Valve, *Phys. Rev. Appl.* **9**, 054002 (2018).
- [31] C. O. Avci, K. Garelo, M. Gabureac, A. Ghosh, A. Fuhrer, S. F. Alvarado, and P. Gambardella, Interplay of spin-orbit torque and thermoelectric effects in ferromagnet/normal-metal bilayers, *Phys. Rev. B* **90**, 224427 (2014).
- [32] S. Y. Huang, W. G. Wang, S. F. Lee, J. Kwo, and C. L. Chien, Intrinsic Spin-Dependent Thermal Transport, *Phys. Rev. Lett.* **107**, 216604 (2011).
- [33] M. Schmid, S. Srichandan, D. Meier, T. Kuschel, J.-M. Schmalhorst, M. Vogel, G. Reiss, C. Strunk, and C. H. Back, Transverse Spin Seebeck Effect versus Anomalous and Planar Nernst Effects in Permalloy Thin Films, *Phys. Rev. Lett.* **111**, 187201 (2013).
- [34] K.-D. Lee, D.-J. Kim, H. Yeon Lee, S.-H. Kim, J.-H. Lee, K.-M. Lee, J.-R. Jeong, K.-S. Lee, H.-S. Song, J.-W. Sohn, S.-C. Shin, and B.-G. Park, Thermoelectric signal enhancement by reconciling the spin Seebeck and anomalous Nernst effects in ferromagnet/non-magnet multilayers, *Sci. Rep.* **5**, 10249 (2015).
- [35] J. Bass and W. P. Pratt, Spin-diffusion lengths in metals and alloys, and spin-flipping at metal/metal interfaces: An experimentalist's critical review, *J. Phys.: Condens. Matter* **19**, 183201 (2007).
- [36] K. Ueda, T. Koyama, R. Hiramatsu, D. Chiba, S. Fukami, H. Tanigawa, T. Suzuki, N. Ohshima, N. Ishiwata, Y. Nakatani, K. Kobayashi, and T. Ono, Temperature dependence of carrier spin polarization determined from current-induced domain wall motion in a Co/Ni Nanowire, *Appl. Phys. Lett.* **100**, 202407 (2012).
- [37] Q. Hao and G. Xiao, Giant spin Hall effect and magneto-transport in a Ta/CoFeB/MgO layered structure: A temperature dependence study, *Phys. Rev. B* **91**, 224413 (2015).
- [38] K.-J. Kim, T. Li, S. Kim, T. Moriyama, T. Koyama, D. Chiba, K.-J. Lee, H.-W. Lee, and T. Ono, Possible contribution of high-energy magnons to unidirectional magnetoresistance in metallic bilayers, *Appl. Phys. Express* **12**, 063001 (2019).
- [39] Y. Lv, J. Kally, D. Zhang, J. S. Lee, M. Jamali, N. Samarth, and J.-P. Wang, Unidirectional spin-Hall and Rashba–Edelstein magnetoresistance in topological insulator-ferromagnet layer heterostructures, *Nat. Commun.* **9**, 111 (2018).
- [40] A. Boehnke, M. Walter, N. Roschewsky, T. Eggebrecht, V. Drewello, K. Rott, M. Münzenberg, A. Thomas, and G. Reiss, Time-resolved measurement of the tunnel magneto-Seebeck effect in a single magnetic tunnel junction, *Rev. Sci. Instrum.* **84**, 063905 (2013).
- [41] L. Liu, C. F. Pai, Y. Li, H. W. Tseng, D. C. Ralph, and R. A. Buhrman, Spin-torque switching with the giant spin Hall effect of tantalum, *Science* **336**, 555 (2012).
- [42] M. Morota, Y. Niimi, K. Ohnishi, D. H. Wei, T. Tanaka, H. Kontani, T. Kimura, and Y. Otani, Indication of intrinsic spin Hall effect in  $4d$  and  $5d$  transition metals, *Phys. Rev. B* **83**, 174405 (2011).
- [43] J.-C. Rojas-Sánchez, N. Reyren, P. Laczkowski, W. Savero, J.-P. Attané, C. Deranlot, M. Jamet, J.-M. George, L. Vila, and H. Jaffrès, Spin Pumping and Inverse Spin Hall Effect in Platinum: The Essential Role of Spin-Memory Loss at Metallic Interfaces, *Phys. Rev. Lett.* **112**, 106602 (2014).
- [44] O. Mosendz, V. Vlaminck, J. E. Pearson, F. Y. Fradin, G. E. W. Bauer, S. D. Bader, and A. Hoffmann, Detection and quantification of inverse spin Hall effect from spin pumping in permalloy/normal metal bilayers, *Phys. Rev. B* **82**, 214403 (2010).
- [45] C. Hahn, G. de Loubens, O. Klein, M. Viret, V. V. Naletov, and J. Ben Youssef, Comparative measurements of inverse spin Hall effects and magnetoresistance in YIG/Pt and YIG/Ta, *Phys. Rev. B* **87**, 174417 (2013).
- [46] Y.-T. Liu, T.-Y. Chen, T.-H. Lo, T.-Y. Tsai, S.-Y. Yang, Y.-J. Chang, J.-H. Wei, and C.-F. Pai, Determination of Spin-Orbit-Torque Efficiencies in Heterostructures with In-Plane Magnetic Anisotropy, *Phys. Rev. Appl.* **13**, 044032 (2020).